



Fractal dimension of large aggregates under different flocculation conditions



Rodrigo B. Moruzzi^{a,*}, André L. de Oliveira^a, Fabiano T. da Conceição^a, John Gregory^b, Luiza C. Campos^b

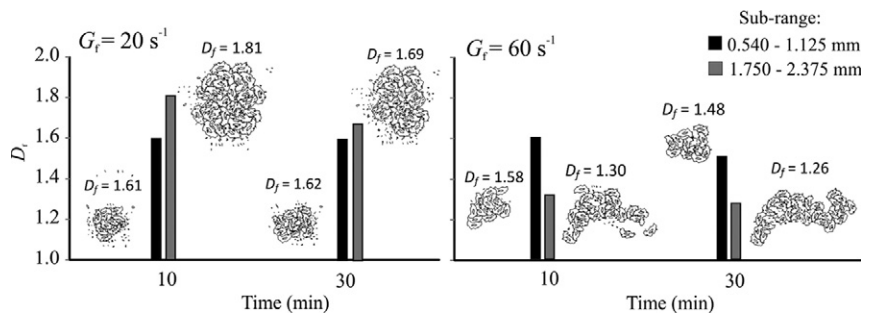
^a Universidade Estadual Paulista (UNESP), Instituto de Geociências e Ciências Exatas, Brazil

^b Department of Civil, Environmental and Geomatic Engineering, University College London, United Kingdom

HIGHLIGHTS

- Large aggregates were monitored by means of size and fractal dimension (2D), using a non-intrusive image system.
- Size range within large aggregates domain results in different behavior of aggregates over time and shear rates.
- Breakage and restructuring play an important role on large aggregates.
- Structure behavior of aggregates may be explained by aggregation mechanisms.

GRAPHICAL ABSTRACT



ARTICLE INFO

Article history:

Received 8 May 2017

Received in revised form 21 July 2017

Accepted 21 July 2017

Available online 30 July 2017

Editor: D. Barcelo

Keywords:

Flocculation

Fractal dimension

Shear rate

Aggregates

ABSTRACT

The two-dimensional fractal dimension (D_f) of large aggregates of kaolin ($>540 \mu\text{m}$) during the shear flocculation process for kaolin solution was investigated using non-intrusive in situ image-based acquisition system. Separate experiments were also carried out for three different sized sub-ranges of large aggregates (0.540–1.125 mm; 1.125–1.750 mm; 1.750–2.375 mm). Digital images were taken at a frequency of 10 Hz for 10 s for each different pairs of gradients of velocity (G_f) of 20 and 60 s^{-1} and flocculation times of 2; 3; 4; 5; 10; 20; 30; 60; 120 and 180 min. For the same conditions, particle size distribution (PSD) was also determined. Under the investigated conditions, the lowest G_f produced the greatest D_f (1.69) at a flocculation time of 30 min for the whole range of aggregates. Also, the evolution of the longest length of aggregate (l) and D_f with time, showed that the dynamic steady-state was reached at different times for each shear rate and l ranges. However, D_f varied for each size sub-range (ca. 1.1 to 1.8). Finally, the behavior of the aggregate structure may be understood by the predominance of different aggregation mechanisms such as cluster-cluster for G_f of 60 s^{-1} and particle-cluster for G_f of 20 s^{-1} .

© 2017 Elsevier B.V. All rights reserved.

1. Introduction

Solid and liquid separation is an essential step in drinking water treatment which primarily depends on particle characteristics of water. These particles exist in all size increments; no matter how

many sub-ranges one divides the entire size range (Lawler, 1997), and they usually cannot be removed before coagulation and flocculation processes. Coagulation destabilizes particles while flocculation is responsible for particle aggregation which occurs with the majority of particles by means of shear-induced collision and orthokinetic aggregation. During this step, it is desirable that destabilized colloids (5.10^{-3} to $1 \mu\text{m}$) are in collision to form larger aggregates (flocs), thus altering mass, surface area, number and morphology as a function of shear rate and time. Large aggregates are defined by Becker et al. (2009) as

* Corresponding author at: 1 – Avenida 24-A, No. 1515, C. P. 178, Bela Vista, CEP 13506-900 Rio Claro, São Paulo, Brazil.

E-mail address: rmoruzzi@rc.unesp.br (R.B. Moruzzi).

aggregates formed from >305 heterogeneous primary particles. So, the aggregate size can indicate the stage of flocculation, once it is expected that aggregate moves from small to large size ranges.

The dynamic steady-state is expected during flocculation for a given shear rate, as aggregation and breakage rates make particle size distribution (PSD) and particle structure stable over time (Jarvis et al., 2005). In this dynamic stage of equilibrium, aggregate size does not change significantly but fluctuates within a certain range, which can be either narrow or broad (He et al., 2012), depending on the applied shear rate and floc strength. Considering the same primary particles (i.e. colloids) under a fixed coagulation condition (e.g. pH and coagulant dosage), the time at which the dynamic steady-state is reached is influenced by both shear rate and aggregate characteristics. This is due to the fact the migration (displacement) of particles in size sub-ranges depends on the dominant flocculation mechanism upon each aggregate size responsible for aggregation and breakage (erosion or fragmentation, depending on either viscous or inertial energy dissipation sub-range). However, aggregates may have the same size but different structures due to different arrangements of particles during aggregation (Vahedi and Gorczyca, 2012).

Thus, the structural characteristic of aggregates should be also relevant for the comprehension of the flocculation process. Gregory (2009) pointed out that aggregates are recognized as fractal objects and that fractal structure has important practical implications, e.g. as aggregate density. Other studies (He et al., 2012; Spicer and Pratsinis, 1996) have demonstrated how flocculation is influenced by the aggregate structure through the representation of fractal dimension. Yang et al. (2013) proposed a combination of the Smoluchowski model of flocculation with fractal theory in replacement of Euclidean geometry to represent particle size. Also, it is suggested that the formation of large aggregates is not enough to guarantee an improvement of the terminal sedimentation velocity, once it can vary with fractal dimension (Chakraborti et al., 2000; Gregory, 1997; Johnson et al., 1996; Vahedi and Gorczyca, 2012).

Several factors may affect fractal structures such as mixing (Logan and Kilps, 1995), pH and coagulant dosage (Xu et al., 2010, 2011), once floc strength is highly dependent on the floc formation process (He et al., 2012). Gregory (2009) also indicated that aggregates formed by perikinetic mechanisms have fractal dimensions lower than those formed during orthokinetic flocculation. It is known that larger aggregates, formed during sweep-coagulation, have higher size and fractal dimensions (Kim et al., 2001; Li et al., 2006) compared to the ones formed during charge neutralization. It is expected that these aggregates have better performance during sedimentation since the terminal velocity is dependent on aggregate size and porosity (Johnson et al., 1996). Also, since the settling velocity varies with the fractal dimension, size is not enough to explain terminal velocity and particle removal by sedimentation (Johnson et al., 1996; Vahedi and Gorczyca, 2012).

Theoretically, self-similar and scale invariants are the most important characteristics of fractal objects (Gregory, 1997; Johnson et al., 1996). However, aggregates in natural systems do not generally follow the theoretical scaling laws, but it is expected this concept is valid for large aggregates with size much bigger than primary particles (Chakraborti et al., 2003). Furthermore, large aggregates are likely to have a different structures and size changes during flocculation as the factors that control their formation are more complex (Vahedi and Gorczyca, 2012).

Becker et al. (2009) used simulation to investigate aggregate behavior based on inter-particle forces and bending moments. The simulations pointed out that for small aggregates, formed by 55 primary particles (named as Aggregate I), stress forces are not sufficient to overcome both bond and bending resistance, so that aggregates remain unchanged and rotating as a rigid body. On the other hand, for very large aggregates, formed by 1000 primary particles, (named as Aggregate III) they will break if they are exposed to shear flows. For aggregates of intermediate size, formed by 305 primary particles (named as

Aggregate II), the structure of aggregates change as consequence of primary particles rearrangements. For this intermediate case, shear forces are high enough to promote aggregate restructuring but not high enough to break primary particles in small fragments.

There is no literature reporting temporal characteristic of aggregates, restricted to large size domain, in terms of fractal dimension evolution. So, the main question is what are the main characteristics of these large aggregates in different shear rates, flocculation times and size sub-ranges? The aim of this study was to investigate the temporal evolution of two-dimensional fractal dimensions of large aggregates in different size ranges from a series of flocculation tests (shear rates of 20 and 60 s⁻¹ and mixing times ranging from 2 to 180 min). The evolution of PSD and the two-dimensional fractal dimensions were all measured by a non-intrusive image analysis. The results may provide new insight into solid and liquid separation processes where the domain of large aggregates is the deciding factor in the sedimentation performance.

2. Materials and methods

2.1. Kaolin suspension

Water was prepared from a stock solution of kaolin suspension based on the studies by Pádua (1994), and Yukselen and Gregory (2004). A commercial kaolin (Sigma-Aldrich) was used as primary particles. The structure composition of dry kaolin was identified by X-ray diffractometry (XRD—Siemens D5000), using a wide-angle X-ray diffractometer, operating at 40 kV and 40 mA, with CuK α radiation. In addition, the surface characterization of the kaolin particles was determined by a JEOL JSM-6010LA scanning electron microscope (SEM), equipped with integrated Energy Dispersive Spectroscopy (EDS) Dry SD Hyper (EX-94410T1L11). A MALVERN Mastersizer 2000 was used to determine the size distribution of the particles. Two-dimensional fractal dimension of dry kaolin particles was determined through the same methodology used for large aggregates described below in Section 2.2, while the images were taken by SEM. In total, 138 primary particles were analyzed.

Kaolin solution was used as representative of clay suspension, differently of uniform-sized spheres reported by Chakraborti et al. (2003). The stock solution turbidity was around 5000 \pm 200 NTU. Stock solution (10 mL) was diluted in deionized water to produce 2 L of water with a turbidity of 25 \pm 2 NTU. Analytic alum (Al₂(SO₄)₃ · 14H₂O) from Sigma was used as coagulant and dosages were presented as Al³⁺. Analytic sodium bicarbonate (NaHCO₃) was used as the buffer during coagulation tests.

2.2. Jar-tests and image capture

Jar-tests were performed as recommended by Yukselen and Gregory (2004) and the jar was coupled to a non-intrusive image capturing system (Fig. 1). All tests were carried using the same jar (Ethik technology Model 218/6 LDB) and at room temperature at 20 \pm 2 °C.

Optimum conditions for coagulation-flocculation were taken from de Oliveira et al. (2015) for image acquisition tests. Therefore, coagulant dosage and solution pH after coagulation were kept constant at 2 mg Al³⁺/L and 7.5, respectively, and coagulation velocity gradient (G_{rm}) and mixing time were 800 s⁻¹ and 10 s, respectively. Velocity gradients (G_f) for flocculation were varied from 20 to 60 s⁻¹ with time (T_f) of 1, 2, 3, 4, 5, 10, 20, 30, 60, 120 and 180 min. However, the 100 samples collected at 1 min were not used once image resolutions were out of the range recommended by Chakraborti et al. (2003). For this reason, only samples collected from 2 min onwards were used. Velocity gradients were previously calibrated by a torque gauge, thus permitting quoting of velocity gradients by means of the equipment's rotation (rpm). Alum was used because it is the most widely used coagulant (Sahu and Chaudhari, 2013) and velocity gradients and flocculation time

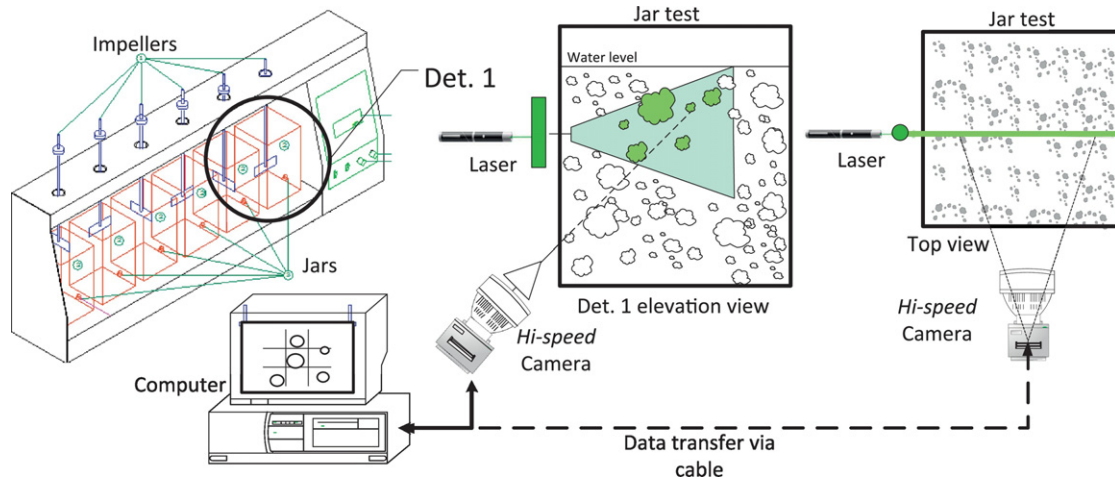


Fig. 1. Schematic representation of the experimental device. Tests were carried out using the same jar. Adapted from Oliveira et al. (2015).

(Table 1) were chosen based on usual range used in treatment process (Chakraborti et al., 2003).

Images were taken at a frequency of 10 Hz for 10 s using the camera coupled to a set of lenses that allowed for an 840 pixel × 640 pixel resolution with a 30 μm pixel size. The *Image-Pro Plus*® software was used to develop the images, i.e. conversion from 2⁸ to 2¹ bits, enhancement and measurement. A laser light sheet of 2000 mW with a 532 nm wavelength and 2 mm thickness was used as an illumination source, in order to obtain good contrast and to define a spatial position for image acquisition. The laser light was accurately adjusted by the focus of the image capture system to allow acquisition control at the middle height of the jar. The main advantage of this non-intrusive method is that the samples can be analyzed without risk of the deformation of flocs due to breakage.

For the PSD analyses, 20 jar-test samples were evaluated. The longest length (*l*) of aggregates was used to determine the relative proportions of the images. So, a continuous function of PSD (Lawler, 1997) was obtained by adjusting Eq. (1) to experimental results, using particle ranges from 0.540 to 2.375 mm.

$$\frac{dN}{d(d_p)} = k(d_p)^{-\beta} \quad (1)$$

where: *k* = power law density coefficient (dimensionless); *d_p* = geometric average of the sub-range where aggregates were classified (mm); *β* = power law slope coefficient (dimensionless).

The same image acquisition system was used to determine the two-dimensional fractal dimension (*D_f*), based on the power law relationship given by Eq. (2). For each condition, *D_f* values were determined from the slope of regression line and longest length (*l*) on a log-log plot (Johnson et al., 1996). However, *D_f* was calculated using aggregates larger than 0.540 mm for the entire range (0.540 to 2.375 mm) and for

three size sub-ranges (sub-range 1: 0.540 to 1.125 mm; sub-range 2: 1.125 to 1.750 mm; sub-range 3: 1.750 to 2.375 mm). For these size sub-ranges, image resolution (*l*/pixel ratio) was between 5.2 and 7.5 thus resulting in an average area ratio around 1.3–1.1 (Chakraborti et al., 2003). More information on image acquisition and processing procedures can be found in Moruzzi and Reali (2007, 2010).

$$A \sim l^{D_f} \quad (2)$$

where: *A* = aggregate area (mm²); *l* = characteristic length of the aggregate, here the longest length was used (mm); *D_f* = two-dimensional fractal dimension (dimensionless).

At this point, it is important to make clear the difference between the characteristic dimensions *d_p* and *l*. Here, *d_p* of Eq. (1) is the geometric mean of the classification range, i.e. it represents the geometric average for each classification interval, using the average length of the aggregates. These average length measures were taken at 2° intervals around the centroid of each one of the aggregates. The *l* used in Eq. (2) is the longest length for each floc, and its variant *l_m* is the average of the longest length. So, *d_p* comes from the discrete classification of data while *l* comes from the longest length and *l_m* is the average of all the raw data.

For each shear rate, the Kolmogorov microscale was calculated using Eq. (3) (Spicer and Pratsinis, 1996).

$$\eta = \left(\frac{\nu}{G}\right)^{\frac{1}{2}} \quad (3)$$

where: *η* = Kolmogorov microscale (m); *ν* = kinematic viscosity of water (m² s⁻¹); *G* = gradient of velocity (s⁻¹).

Table 1

Characterization of large aggregates for the whole sample (0.540 to 2.375 mm) for ten flocculation times (*T_f*) and two shear rates (*G_f*). *η* is the Kolmogorov microscale. *l_m* is the median size for the longest dimension of the whole distribution of large aggregates (mm). *D_f* is the two-dimensional fractal dimension. Numbers within parentheses are standard deviation values of *D_f* and *l_m*.

<i>G_f</i> (s ⁻¹)	<i>η</i> (μm)		<i>T_f</i> (min)									
			2	3	4	5	10	20	30	60	120	180
20	239 ± 13	<i>l_m</i>	0.67 (0.12)	0.70 (0.20)	0.70 (0.22)	0.78 (0.29)	0.97 (0.45)	0.94 (0.44)	0.90 (0.39)	0.85 (0.34)	0.81 (0.27)	0.80 (0.31)
		<i>D_f</i>	1.17 (0.22)	1.29 (0.10)	1.16 (0.20)	1.54 (0.07)	1.68 (0.18)	1.68 (0.11)	1.69 (0.10)	1.48 (0.28)	1.52 (0.18)	1.56 (0.12)
		<i>R</i> ²	0.90	0.86	0.84	0.87	0.90	0.89	0.89	0.88	0.86	0.87
60	138 ± 07	<i>l_m</i>	0.83 (0.38)	0.74 (0.27)	0.74 (0.26)	0.76 (0.30)	0.68 (0.24)	0.74 (0.25)	0.68 (0.22)	0.70 (0.23)	0.68 (0.23)	0.68 (0.21)
		<i>D_f</i>	1.41 (0.05)	1.36 (0.05)	1.40 (0.10)	1.43 (0.04)	1.38 (0.11)	1.35 (0.06)	1.32 (0.09)	1.31 (0.06)	1.30 (0.08)	1.28 (0.08)
		<i>R</i> ²	0.86	0.82	0.81	0.82	0.79	0.81	0.8	0.83	0.82	0.82

3. Results and discussion

3.1. Kaolin characterization

X-ray diffraction (XRD) patterns of dry kaolin used in this study is shown in Fig. 2a. It can be seen that this material is composed mainly of kaolinite ($\text{Al}_2\text{Si}_2\text{O}_5(\text{OH})_4$), illite [$\text{K}_{0.9}\text{Al}_2\text{Si}_4\text{O}_{10}(\text{OH})_2 \cdot (\text{H}_2\text{O})$] and microcline (KAlSi_3O_8). It also consists of kaolinite plates and particles of different size, shape and texture (Fig. 2b). The particle size distribution (Fig. 2c) of this raw material indicates a heterogeneous size range, varying from lower than $1\ \mu\text{m}$ up to higher than $100\ \mu\text{m}$ of diameter, with a median of $7.5\ \mu\text{m}$. The fractal dimension (D_f) of kaolin was around 1.54, indicating the natural flat surface of this material (Malekani et al., 1996).

3.2. Particle size distribution of aggregates

During coagulation-flocculation tests 2000 images were taken capturing ca. 465,000 aggregates and resulting in a sample error of $<1\%$ for 99% reliability. In Fig. 3 is shown an example of one raw image, i.e.

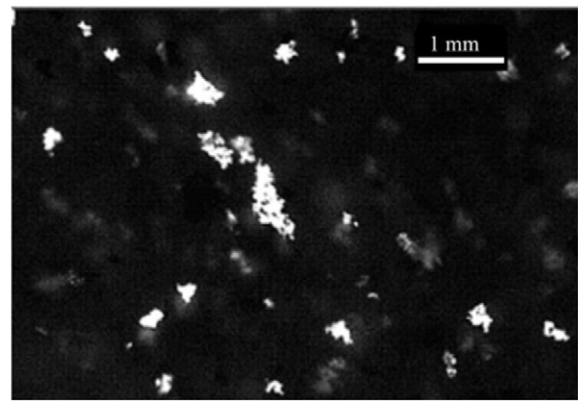


Fig. 3. Example of raw image (as captured) of aggregates taken at monochromatic mode with 2^8 bits, pixel of $30\ \mu\text{m}$.

as taken by the image system. In total, 16 particle size classes were obtained from the limit of 0.540 to $2.375\ \text{mm}$. Within each size class the diameter of the geometric mean was used to classify aggregate size.

The adjustment of the log-log plot of Eq. (1) can be observed in Fig. 4 for G_f of 20 and $60\ \text{s}^{-1}$ in flocculation time (T_f) of $2, 5$ and $180\ \text{min}$. Considering the initial range of size of kaolin (particles ranging from lower than $1\ \mu\text{m}$ up to higher than $100\ \mu\text{m}$ of diameter, with a median of $7.5\ \mu\text{m}$), there was clearly a particle displacement from the lowest to the highest sub-ranges of size caused by flocculation for both G_f values here exemplified. However, for G_f of $20\ \text{s}^{-1}$ (Fig. 4a), the transition of small particles from low to high sub-ranges took more time. This can be observed by means of the slope of the adjusted curves for T_f of $2\ \text{min}$ (Fig. 4a and b). For G_f of $60\ \text{s}^{-1}$, there were fewer large flocs (high slope). These behaviors were expected due to the flocculation kinetics where aggregation rate and aggregate size are dependent of G_f

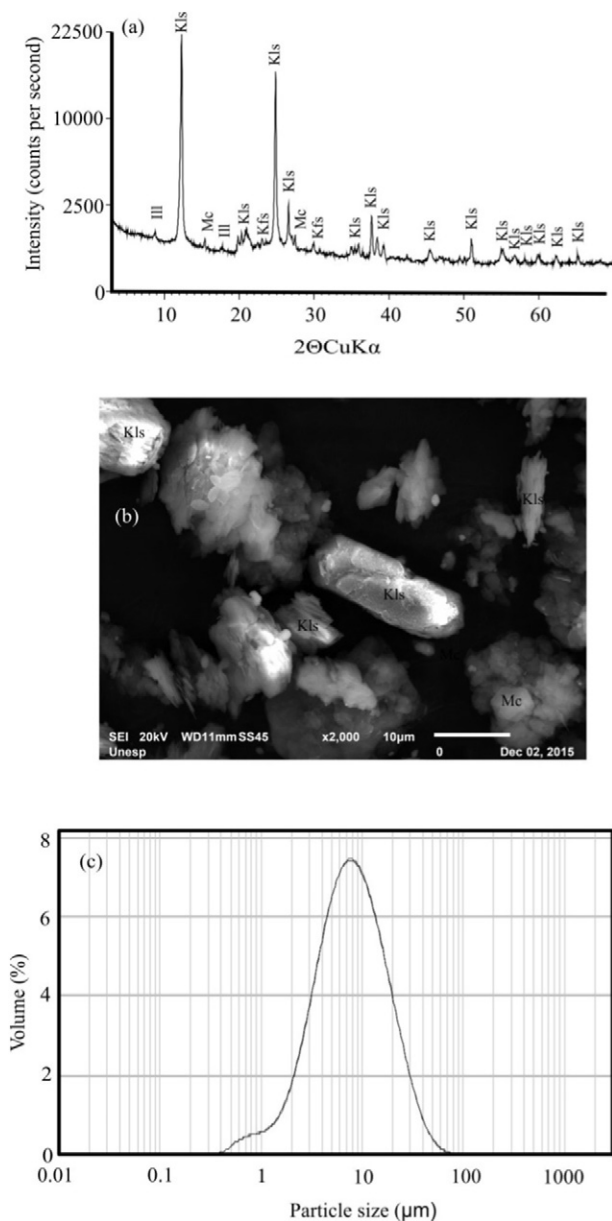


Fig. 2. XDR characterization (a), SEM-EDS (b) and particle size distribution (c) of commercial kaolin. Kaolinite = Kln, Illite = Ill and Mc = microcline.

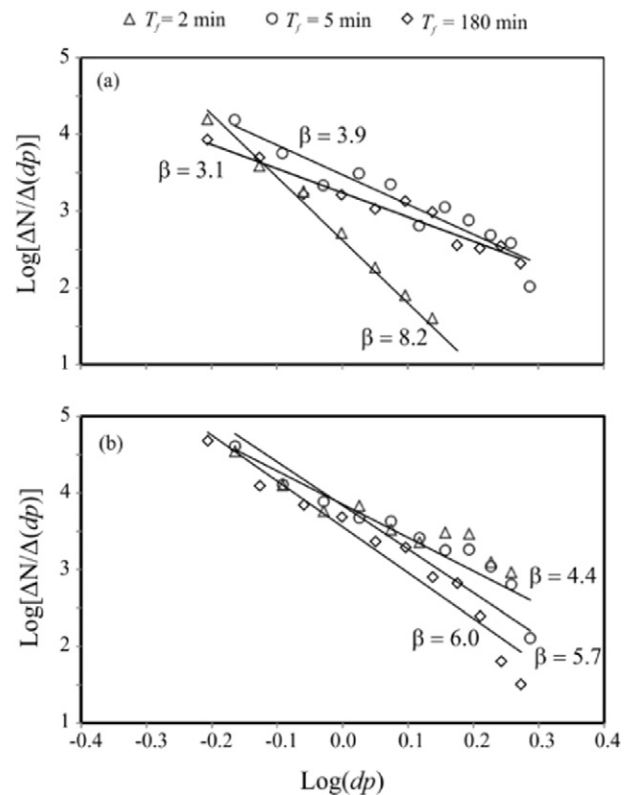


Fig. 4. Example of large aggregate size distribution written as log-log plot of Eq. (1) for three flocculation times. The slope of the trend line gives the β value. (a) $G_f = 20\ \text{s}^{-1}$ and $T_f = 2, 5$ and $180\ \text{min}$. (b) $G_f = 60\ \text{s}^{-1}$ and $T_f = 2, 5$ and $180\ \text{min}$.

(Jarvis et al., 2005). For all tests, the power law slope coefficient β values started from around 8 for G_f of 20 s^{-1} and 6 for G_f of 60 s^{-1} , reaching a minimum value for a T_f of 5 min and then increasing again for a T_f of 180 min.

3.3. Characterization of the whole population of large aggregates

The images of flocs formed for shear rates of 20 and 60 s^{-1} in different flocculation times were analyzed and the two-dimensional fractal dimension (D_f) for the whole population of large aggregates was derived as shown in Table 1. According to Waite (1999), D_f is usually an integer number for Euclidean objects, but D_f values do not follow Euclidean geometry for fractal objects. More circular aggregates have a greater fractal dimension (closer to 2), while aggregates with a looser structure have a smaller fractal dimension (closer to 1). The median of the longest dimension for aggregate size for the whole distribution (l_m), Kolmogorov microscale (η) and the R^2 value for log-log slope can be seen in Table 1. Once the l_m represents the median of the longest length of aggregates, it is influenced by the relative frequency in each size range. This measure is influenced by asymmetry as frequency of low sub ranges is more pronounced. D_f values were calculated based on the whole large aggregate sample ($>0.540\text{ mm}$), which is formed by >305 primary particles. Standard deviations for each D_f value are given in parentheses. A statistical analysis of the all the experimental data indicated that D_f values were statistically different ($p < 0.05$) after 10 min of flocculation time.

For both shear rates studied, aggregate size (l_m) values are above the Kolmogorov microscale ($\eta < 540\text{ }\mu\text{m}$) suggesting that breakage mostly occurs by fragmentation (He et al., 2012; Thomas et al., 1999). For 20 s^{-1} , the median aggregate size increased from 0.67 to 0.97 mm during the first stage of flocculation (2 to 10 min), after which decreasing until a value of 0.80 mm was reached at 180 min. On the other hand, l_m values rapidly reached the maximum value of 0.83 mm at 2 min for G_f of 60 s^{-1} and then decreases over time to the final value of 0.68 mm at 180 min.

Referring to the evolution of two-dimensional fractal dimension, at a shear rate of 20 s^{-1} , D_f values increased during the first 10 min, stabilized over 10 to 30 min, reached the highest value (i.e. 1.69) at 30 min, decreased to 1.48 at 60 min and increased up to 1.56 at 180 min. However, for G_f of 60 s^{-1} D_f values decreased with time from 1.41 (T_f of 2 min) to 1.28 (T_f of 180 min), similar to the observations made by Chakraborti et al. (2003). D_f values were 1.32 (G_f of 60 s^{-1}) and 1.69 (G_f of 20 s^{-1}) at 30 min, and these are in agreement with those values reported by Li et al. (2007). R^2 values ranged from 0.79 to 0.90, indicating a good fit for the log-log plot of the whole population of aggregates, in terms of area and size (l).

The steady state was reached around 30 min for both l_m and D_f for G_f equal to 60 s^{-1} . In contrast, for a G_f equal to 20 s^{-1} the plateau was reached only after a T_f of 60 min which corroborates well with Spicer and Pratsinis (1996), Chakraborti et al. (2003) and He et al. (2012). Furthermore, comparing results from Fig. 3 and Table 1, it can be observed that D_f varied while β was stable after T_f of 5 min. This emphasizes that PSD may not be enough to evaluate flocculation of large aggregates, since aggregate size and structure are both modified and the steady state may occur differently depending on size and structure of aggregates (Vahedi and Gorczyca, 2012). Also, PSD (or even l) is influenced by small particles and thus the identification of changes in large aggregates may not be accurate.

The relation between l_m and D_f obtained in this study seems to contradict those reported by Chakraborti et al. (2003) and Li et al. (2007), who found that higher D_f were observed for higher G_f (80 s^{-1}) i.e. lower aggregate sizes. In this study, higher D_f values were observed for G_f of 20 s^{-1} after T_f of 10 min which means higher aggregate sizes. This contradiction may be because the present work has considered only aggregates of large size and small aggregates influence the D_f

values when the slope of log-log plot is used for a population of aggregates (Chakraborti et al., 2003).

3.4. Aggregate characteristics within size sub-range

In order to check the influence of G_f and T_f for different size sub-ranges, D_f values for each one of the investigated sub-ranges were calculated. However, before presenting D_f results, it is important to show the temporal evolution of the absolute and relative frequency of each sub-range at the two investigated shear rates, since restructuring, fragmentation and reformation may also alter the aggregate size. Ten flocculation times were tested for each velocity gradient (from 2 to 180 min), and different numbers of aggregates (N) were taken each time due to the random sampling procedure (Table 2).

Fig. 5 shows the frequency in relative numbers of large aggregates within three size sub-ranges at ten sampling times and two shear rates. Aggregates in the sub-range 1 from 0.540 to 1.125 mm were predominant for both shear rates at all sampling times, thus explaining the proximity of the average of l (i.e., l_m) values in Table 1. However, it can be seen up to 30% of aggregates in the sub-range 3 from 1.175 to 2.375 mm at a shear rate of 20 s^{-1} and between 10 and 30 min. Relatively, the amount of aggregates decreased at the sub-range 3 (1.750 to 2.375 mm) for G_f of 60 s^{-1} .

Fig. 6 shows the D_f values at three size sub-ranges within the large domain of aggregate ($>0.540\text{ mm}$) for ten sampling times and two shear rates. For all sampling times, D_f varied from ~ 1.1 to 1.8 for all size sub-ranges, confirming that D_f for large aggregates varies widely (Vahedi and Gorczyca, 2012). Similar to the results presented in Table 1, Fig. 6 shows that D_f values varied with time, and the time at which dynamic steady state was reached was different from those observed when the whole large domain was considered. In general, it is important to note that D_f tended to be greater for lower size sub-ranges and vice versa, confirming the idea that the restructuring of large aggregates may result in more compact flocs.

It is still possible to see in Fig. 6 that for the sub-range 1 (0.540 to 1.125 mm), aggregates rapidly reach a plateau at around 20 min, and then values fluctuated in a range of $\pm 8\%$. On the other hand, it took about 30 min for the sub-range 2 to reach a plateau and the values fluctuated over a wider range ($\pm 30\%$) than the sub-range 1. In addition, D_f also varied in a wider range for sub-range 3, especially for time < 60 min.

Table 2
Number of aggregates (N) for each sampling time and size sub-range at G_f of 20 and 60 s^{-1} .

Time (min)	Number of aggregates			
	0.540–1.125 mm	1.125–1.750 mm	1.750–2.375 mm	Total
<i>G_f of 20 s⁻¹</i>				
2	12,837	303	14	13,154
3	29,437	3353	470	33,260
4	20,077	2440	401	22,918
5	12,753	2537	646	15,936
10	3010	527	1263	4800
20	3363	488	1484	5335
30	3731	504	1534	5769
60	3694	274	1279	5247
120	3805	107	980	4892
180	8466	374	1917	10,757
<i>G_f of 60 s⁻¹</i>				
2	30,786	7820	2570	41,176
3	30,278	5270	1130	36,678
4	26,204	4120	895	31,219
5	27,665	5571	1432	34,668
10	24,776	3490	629	28,895
20	28,924	4699	973	34,596
30	27,366	3486	532	31,384
60	30,466	3978	633	35,077
120	31,487	4077	687	36,251
180	29,629	3419	532	33,580

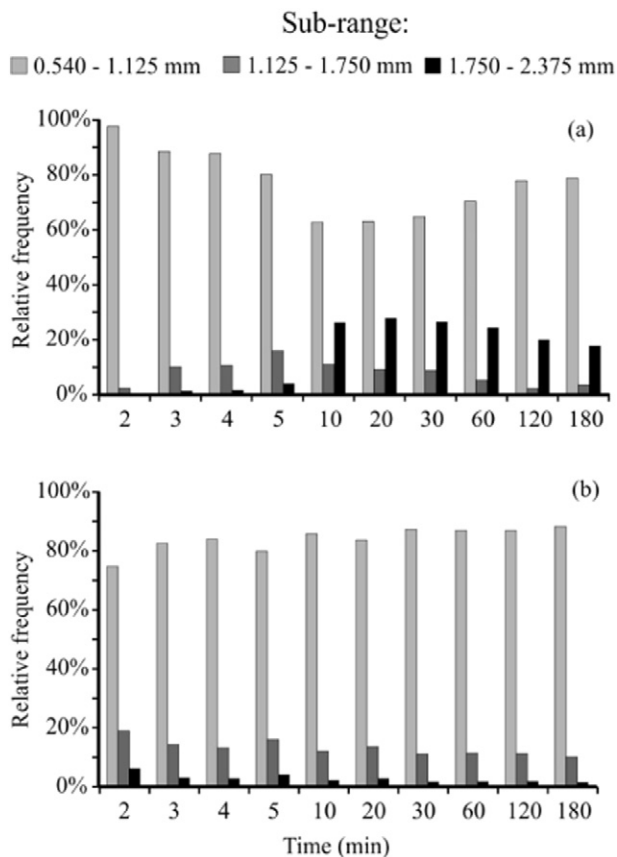


Fig. 5. Relative frequency of analyzed aggregates at ten flocculation times for three size sub-ranges for G_f 20 s^{-1} (a) and 60 s^{-1} (b).

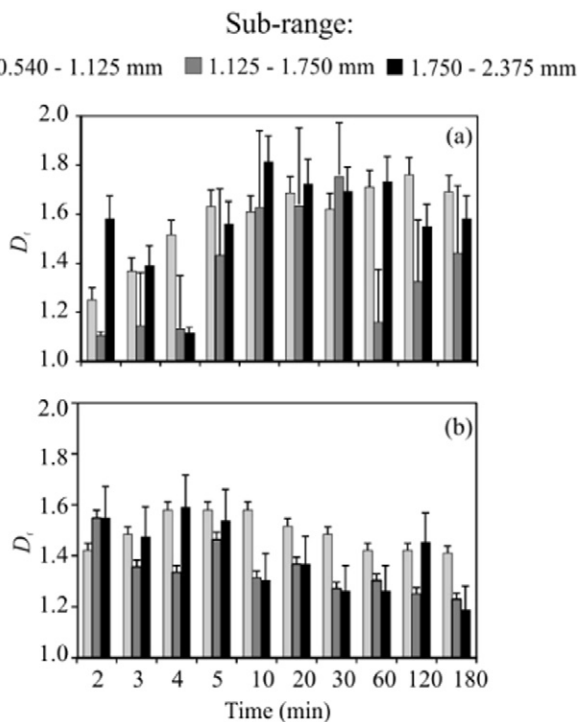


Fig. 6. Evolution of D_f with flocculation time for three size sub-ranges for G_f of 20 s^{-1} (a) and 60 s^{-1} (b). Bars indicate standard deviation for each sub-range (5–30%). In total 2000 images were taken capturing ca. 465,000 aggregates.

In general, the G_f of 20 s^{-1} showed the wider fluctuation for all sub-range samples. This was expected, since for the G_f of 20 s^{-1} there were aggregates in all large size sub-ranges, especially in the widest sub-range (as shown in Fig. 4a), where the mechanisms for complexes govern aggregation and breakage (Vahedi and Górczyca, 2012).

Finally, it can be also seen that D_f values for each sub-range clearly present a peak at different times, and there is an increase followed by a decrease (presented by a peak) as shown in Fig. 6a or there is a simple decrease with time (Fig. 5b), as observed by Chakraborti et al. (2003). However, a huge variation of the D_f values obtained from the samples within different size sub-ranges extracted at the same time was observed, contradicting the results presented by Chakraborti et al. (2003) for aggregates ranging from 10 to $45 \mu\text{m}$, not much larger than the primary particles ($9.975 \pm 0.061 \mu\text{m}$). Here, only a large domain of aggregates was considered for the D_f calculation. Further, here heterodisperse kaolin particles were used, differently to monodisperse microspheres of latex used by Chakraborti et al. (2003). Moreover, it is important to highlight that it is possible that the overestimation of the area for the lower sub-ranges may result in smaller D_f values, when the fractal dimension is calculated using the whole population of aggregates (Chakraborti et al., 2003).

3.5. Evolution of D_f within size sub-ranges of large aggregates

Upon evaluation of the results presented, it has been found that large aggregates behaved differently from the smaller ones reported in the literature (e.g. Chakraborti et al., 2003). Here, large aggregate size (l_m) seemed not to change significantly after the dynamic steady state was reached but their structure, measured by means of D_f , still changed with time. Also, different sub-ranges of large aggregates behaved differently with time, resulting in both different D_f values and steady state position with time. The lower sub-range of the large aggregate domain presented a more stable behavior than the larger sub-ranges.

In general, a broad range of two-dimensional fractal dimension (D_f) was found ~ 1.1 – 1.8 for different size sub-ranges domains, and these ranges for D_f are in agreement with results reported by Chang et al. (2005) and Li et al. (2007). Also, clusters formed from heterodisperse primary particles of kaolin coagulated with Al^{3+} reaching both a greater size and higher D_f values for the lower shear rate investigated (G_f of 20 s^{-1}). This contradicts results obtained from small aggregates, as presented by Chakraborti et al. (2003) and Li et al. (2007). Fig. 7 shows the possible pathways during flocculation of large aggregates domains.

A possible explanation is that a mechanism similar to particle-cluster aggregation (PCA) may occur for low G_f , once there are still significant amounts of primary particles remaining (or even relatively small clusters, that may behave as single particles when precipitate of alum is formed), thus favoring particle attachment into large precipitate clusters of alum precipitate. In this way, primary particles, or small clusters, may adhere into alum precipitate favoring a large D_f . Otherwise, the probability of large D_f values for cluster approximation is near to zero as aggregate size increases, according to predictions made by Brasil et al. (2001). Further, the coagulant type and dose here investigated may overlap the isolated effect of particle and cluster mechanisms for large aggregates, once the properties of flocs are strongly dependent on coagulant dose and type, as described by Yu et al. (2015).

Results also suggest that after aggregation, fragmentation and restructuring may change large aggregates, according to their size and compaction. Becker et al. (2009) studied the behavior of small and large aggregates in shear rates, and represented two possible draw for restructuring of large aggregates (Aggregate II and III). For Aggregate-II, restructuring starts with stretching followed by compaction, and for Aggregate III break up and reformation may occur, thus leading to stronger and more compact flocs. Aggregates formed by shear rate of G_f of 20 s^{-1} might have behaved like Aggregate-II and Aggregate-III, as suggested by Becker et al. (2009). For G_f of 20 s^{-1} an initial stretched phase (lower D_f values) is followed by an aggregate compaction (higher

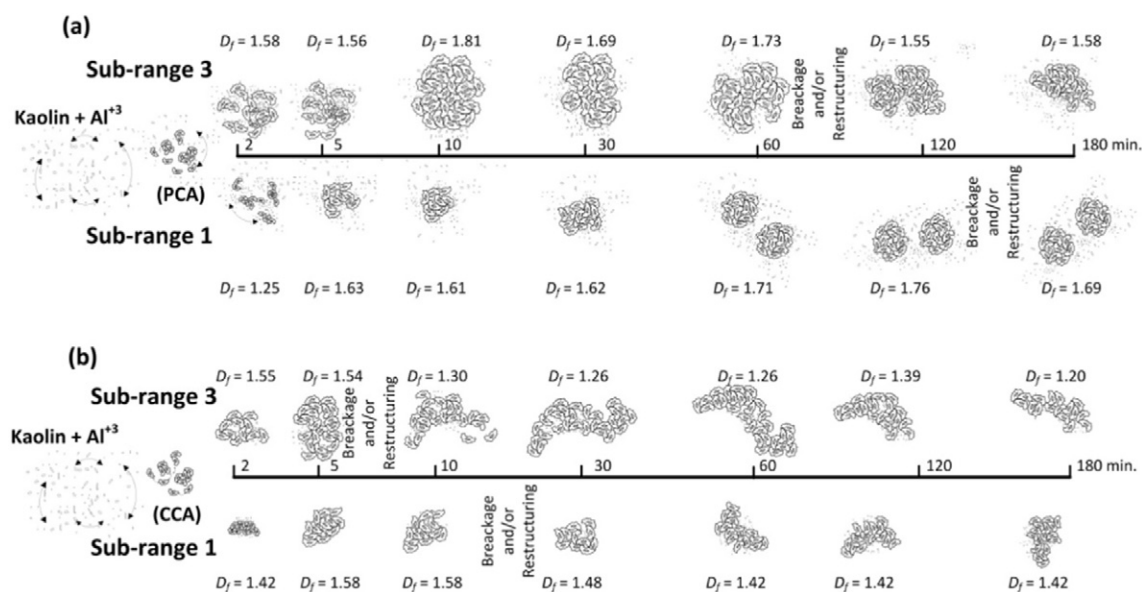


Fig. 7. Schematic of aggregates growth during flocculation for two shear rates: (a) 20 s^{-1} and (b) 60 s^{-1} in two size sub-ranges (sub-range 1 from 0.540 to 1.125 mm and sub-range 3 from 1.750 to 2.375 mm). The values above the flocs represent D_f values.

D_f). Afterward, rupture leading to fragmentation results in a slightly stretched structure.

For G_f of 60 s^{-1} cluster-cluster like aggregation (CCA) may better explain aggregate structures. In this case, aggregates seem to behave more like in reaction-limited domain [slow aggregation, as presented by Lin et al., 1989], when an energy barrier has to be overcome before attaching. Also, formed clusters of large aggregates have shown good agreement with computer simulations presented by Becker et al. (2009). For this shear rate, Aggregate-I seems more appropriate to explain D_f behavior, since a fragmented small cluster may rotate like a rigid body (Becker et al., 2009). The behavior of D_f values for G_f of 60 and 20 s^{-1} may also be explained using the findings reported by Deng and Davé (2017). According to these authors, D_f values strongly depend upon the initial velocities of the aggregates, where higher random velocities lead to more irregular shape, i.e. lower D_f values. Again, alum precipitate may determine aggregate characteristics.

4. Conclusions

The results presented here may provide new insight on two-dimensional fractal dimensions of a large domain of aggregates, which are fundamental to separation processes since large aggregates hold most of the mass of contaminant and the majority of the energy applied in the flocculation process by mixers. The main conclusions of this study are:

- While considering different sub-ranges of large domains, D_f values varied with the lowest range of size, resulting in the highest D_f for each G_f ;
- The growth evolution of the longest length of aggregate (l_m) and the change of the D_f with time demonstrated that the dynamic steady-state was reached, but over different times for each shear rates and size (l_m) ranges;
- D_f values for different times and shear rate were obtained, and the structure behavior of aggregates may be explained by aggregation mechanisms (like cluster-cluster for G_f of 60 s^{-1} and like particle-cluster for G_f of 20 s^{-1}). Also for large aggregates, the complex mechanism of restructuring probably leads to different structures

and D_f . It is possible that precipitated alum determine large aggregates' characteristics.

Acknowledgments

The research was supported by the São Paulo Research Foundation (*Fundação de Amparo à Pesquisa do Estado de São Paulo—FAPESP*). Proc. 2010/50694-0; 2013/25641-9; 2013/21355-1; 2013/01634-3. The authors dedicate this work in memory of Dr. Marcelo De Julio who contributed to the advancement of the coagulation-flocculation research in Brazil.

References

- Becker, V., Schalaus, E., Behr, M., Briesen, H., 2009. Restructuring of colloidal aggregates in shear flows and limitations of the free-draining approximation. *J. Colloid Interface Sci.* 339 (2):362–372. <http://dx.doi.org/10.1016/j.jcis.2009.07.022>.
- Brasil, A.M., Farias, T.L., Carvalho, M.G., Koylu, U.O., 2001. Numerical characterization of the morphology of aggregated particles. *Aerosol Sci.* 32, 489–508.
- Chakraborti, R.K., Atkinson, J.F., Van Benschoten, J.E., 2000. Characterization of alum floc by image analysis. *Environ. Sci. Technol.* 34:3969–3976. <http://dx.doi.org/10.1021/es990818o>.
- Chakraborti, R.K., Gardner, K.H., Atkinson, J.F., Van Benschoten, J.E., 2003. Changes in fractal dimension during aggregation. *Water Res.* 37, 873–883.
- Chang, Y., Liu, Q., Zhang, J., 2005. Flocculation control study based on fractal theory. *J. Zhejiang Univ. Sci.* 10, 1038–1044.
- de Oliveira, A.L., Moreno, P., da Silva, P.A.G., Julio, M.D., Moruzzi, R.B., 2015. Effects of the fractal structure and size distribution of flocs on the removal of particulate matter. *Desalination and Water Treatment*. Taylor & Francis:pp. 1–12 <http://dx.doi.org/10.1080/19443994.2015.1081833>.
- Deng, X., Davé, R.N., 2017. Breakage of fractal agglomerates. *Chem. Eng. Sci.* 161:117–126. <http://dx.doi.org/10.1016/j.ces.2016.12.018>.
- Gregory, J., 1997. The density of particle aggregates. *Water Sci. Technol.* 36, 1–13.
- Gregory, J., 2009. Monitoring particle aggregation processes. *Adv. Colloid Interf. Sci.* 147–148:109–123. <http://dx.doi.org/10.1016/j.cis.2008.09.003>.
- He, W.P., Nan, J., Li, H.Y., Li, S.N., 2012. Characteristic analysis on temporal evolution of floc size and structure in low-shear flow. *Water Res.* 46:509–520. <http://dx.doi.org/10.1016/j.watres.2011.11.040>.
- Jarvis, P., Jefferson, B., Gregory, J., Parsons, S.A., 2005. A review of floc strength and breakage. *Water Res.* 39:3121–3137. <http://dx.doi.org/10.1016/j.watres.2005.05.022>.
- Johnson, C.P., Li, X., Logan, B.E., 1996. Settling velocities of fractal aggregates. *Environ. Sci. Technol.* 30, 1911–1918.
- Kim, S.-H., Moon, B.-H., Lee, H.-I., 2001. Effects of pH and dosage on pollutant removal and floc structure during coagulation. *Microchem. J.* 68, 197–203.
- Lawler, D.F., 1997. Particle size distributions in treatment processes: theory and practice. *Proceedings of the Fourth International Conference: the Role of Particle Characteristics in Separation Processes*. IAWQ–IWSA Joint Specialist Group on Particle Separation, Jerusalem (28–30 October 1996).

- Li, T., Zhu, Z., Wang, D., Yao, C., Tang, H., 2006. Characterization of floc size, strength and structure under various coagulation mechanisms. *Power Technol.* 168:104–110. <http://dx.doi.org/10.1016/j.powtec.2006.07.003>.
- Li, T., Zhu, Z., Wang, D., Yao, C., Tang, H., 2007. The strength and fractal dimension characteristics of alum-kaolin flocs. *Int. J. Miner. Process.* 82, 23–29.
- Lin, M.Y., Lindsay, H.M., Weitz, D.A., Ball, R.C., Klein, R., Meakin, P., 1989. Universality in colloid aggregation. *Nature* 339, 360–362.
- Logan, B.E., Kilps, J.R., 1995. Fractal dimensions of aggregates formed in different fluid mechanical environments. *Water Res.* 29, 443–453.
- Malekani, K., Rice, J.A., Lin, J.S., 1996. Comparison of techniques for determining the fractal dimensions of clay minerals. *Clay Clay Miner.* 44, 677–685.
- Moruzzi, R.B., Reali, M.A.P., 2007. Método para determinação de distribuição de tamanho de microbolhas (DTMB) em sistemas flotação (FAD) para tratamento de águas utilizando a análise de imagem digital [Method for measuring bubbles sizes distribution (BSD) in drinking water treatment flotation (DAF) systems by using digital image analysis]. *Eng. Sanit. Ambient.* 12 (3):273–283. <http://dx.doi.org/10.1590/S1413-41522007000300007>.
- Moruzzi, R.B., Reali, M.A.P., 2010. Characterization of microbubble size distribution and flow configuration in DAF contact zone by a non-intrusive image analysis system and tracer tests. *Water Sci. Technol.* 61 (1):253–262. <http://dx.doi.org/10.2166/wst.2010.784>.
- Pádua, V.L., 1994. Metodologia para determinação dos gradientes de velocidade médios em unidades de floculação de mistura completa com câmaras em série e escoamento contínuo a partir de reatores estáticos [Methodology to Determine Mean Velocity Gradients in Complete Mixture Flocculation Units With Series Chambers and Continuous Flow From Static Reactors]. Thesis (Masters in Hydraulics and Sanitation). São Carlos School of Engineering, University of São Paulo (Escola de Engenharia de São Carlos, Universidade de São Paulo), São Carlos, p. 165.
- Sahu, O.P., Chaudhari, P.K., 2013. Review on chemical treatment of industrial waste water. *J. Appl. Sci. Environ. Manag.* 17 (2), 241–257.
- Spicer, P.T., Pratsinis, S.E., 1996. Shear-induced flocculation: the evolution of floc structure and the shape of the size distribution at steady state. *Water Res.* 30, 1049–1056.
- Thomas, D.N., Judda, S.J., Faucett, N., 1999. Flocculation modelling: a review. *Water Res.* 33 (7), 1579–1592.
- Vahedi, A., Gorczyca, B., 2012. Predicting the settling velocity of flocs formed in water treatment using multiple fractal dimensions. *Water Res.* 46:4188–4194. <http://dx.doi.org/10.1016/j.watres.2012.04.031>.
- Waite, T.D., 1999. Measurement and implications of floc structure in water and wastewater treatment. *Colloids Surf. A* 151, 27–41.
- Xu, W.Y., Gao, B.Y., Yue, Q.Y., Wang, Y., 2010. Effect of shear force and solution pH on flocs breakage and re-growth formed by nano- Al_{13} polymer. *Water Res.* 44:1893–1899. <http://dx.doi.org/10.1016/j.watres.2009.11.029>.
- Xu, W., Gao, B., Yue, Q., Bo, X., 2011. Influence of pH on flocs formation, breakage and fractal properties—the role of Al_{13} Polymer. *J. Water Sustain.* 1 (1), 45–57.
- Yang, Z., Yang, H., Jiang, Z., Huang, X., Li, H., Li, A., Cheng, R., 2013. A new method for calculation of flocculation kinetics combining Smoluchowski model with fractal theory. *Colloids Surf. A Physicochem. Eng. Asp.* 423:11–19. <http://dx.doi.org/10.1016/j.colsurfa.2013.01.058>.
- Yu, W., Gregory, J., Campos, L.C., Graham, N., 2015. Dependence of floc properties on coagulation type, dosing mode and nature of particles. *Water Res.* 68, 119–126.
- Yukselen, M.A., Gregory, J., 2004. The reversibility of floc breakage. *Int. J. Miner. Process.* 73:251–259. [http://dx.doi.org/10.1016/S0301-7516\(03\)00077-2](http://dx.doi.org/10.1016/S0301-7516(03)00077-2).